Chapman University
Chapman University Digital Commons

Biology, Chemistry, and Environmental Sciences Faculty Articles and Research

Biology, Chemistry, and Environmental Sciences

2012

Assessing Satellite-Based Rainfall Estimates In Semiarid Watersheds Using the Usda-Ars Walnut Gulch Gauge Network and Trmm Pr

Eyal Amitai
Chapman University

Carl L. Unkrich
USDA-ARS Southwest Watershed Research Center

David C. Goodrich
USDA-ARS Southwest Watershed Research Center

Emad Habib
University of Louisiana at Lafayette

Bryson Thill
Chapman University

Follow this and additional works at: http://digitalcommons.chapman.edu/sees_articles

Part of the Fresh Water Studies Commons, Hydrology Commons, and the Meteorology Commons

Assessing Satellite-Based Rainfall Estimates In Semiarid Watersheds Using the Usda-Ars Walnut Gulch Gauge Network and Trmm Pr

Assessing Satellite-Based Rainfall Estimates in Semiarid Watersheds Using the USDA-ARS Walnut Gulch Gauge Network and TRMM PR

EYAL AMITAI

NASA Goddard Space Flight Center, Greenbelt, Maryland, and Chapman University, Orange, California

CARL L. UNKRICH AND DAVID C. GOODRICH

USDA-ARS Southwest Watershed Research Center, Tucson, Arizona

EMAD HABIB

University of Louisiana at Lafayette, Lafayette, Louisiana

BRYSON THILL

Chapman University, Orange, California

(Manuscript received 24 January 2012, in final form 21 May 2012)

ABSTRACT

The rain gauge network associated with the Walnut Gulch Experimental Watershed (WGEW) in southeastern Arizona provides a unique opportunity for direct comparisons of in situ measurements and satellite-based instantaneous rain rate estimates like those from the Tropical Rainfall Measuring Mission (TRMM) precipitation radar (PR). The WGEW network is the densest rain gauge network in the PR coverage area for watersheds greater than 10 km^2. It consists of 88 weighing rain gauges within a 149-km^2 area. On average, approximately 10 gauges can be found in each PR field of view (~5-km diameter). All gauges are very well synchronized with 1-min reporting intervals. This allows generating very-high-temporal-resolution rain rate fields and obtaining accurate estimates of the area-average rain rate for the entire watershed and for a single PR field of view. In this study, instantaneous rain rate fields from the PR and the spatially interpolated gauge measurements (on a 100 m × 100 m grid, updated every 1 min) are compared for all TRMM overpasses in which the PR recorded rain within the WGEW boundaries (25 overpasses during 1999–2010). The results indicate very good agreement between the fields with low bias values (<10%) and high correlation coefficients, especially for the near-nadir cases (>0.9). The correlation is high at overpass time but the peak occurs several minutes after the overpass, which can be explained by the fact that it takes several minutes for the raindrops to reach the gauge from the time they are observed by the PR. The correlation improves with the new version of the TRMM algorithm (V7). The study includes assessment of the accuracy of the reference products.

1. Introduction

The evaluation of rainfall rate (R) estimates from low-orbital satellite observations, like for the Tropical Rainfall Measuring Mission (TRMM) (Kummerow et al. 1998), is conventionally performed by comparisons with other remote sensing products (e.g., ground radar fields). Direct comparisons with in situ measurements (e.g., rain gauges) have been limited to rainfall *accumulations*. Such comparisons are associated with large uncertainties due to satellite temporal sampling errors. Comparisons of instantaneous R fields (snapshots) from satellite and gauge observations have been avoided, as they are associated with large uncertainties due to volume sampling discrepancies. However, the configuration of the gauge network in the Walnut Gulch Experimental Watershed (WGEW) (Goodrich et al. 2008) in southeastern Arizona and its high degree of temporal synchronization justify such comparisons.

The objective of this study is to make "instantaneous" rain rate comparisons and to investigate how well both fields compare in the semiarid climate of the southwest
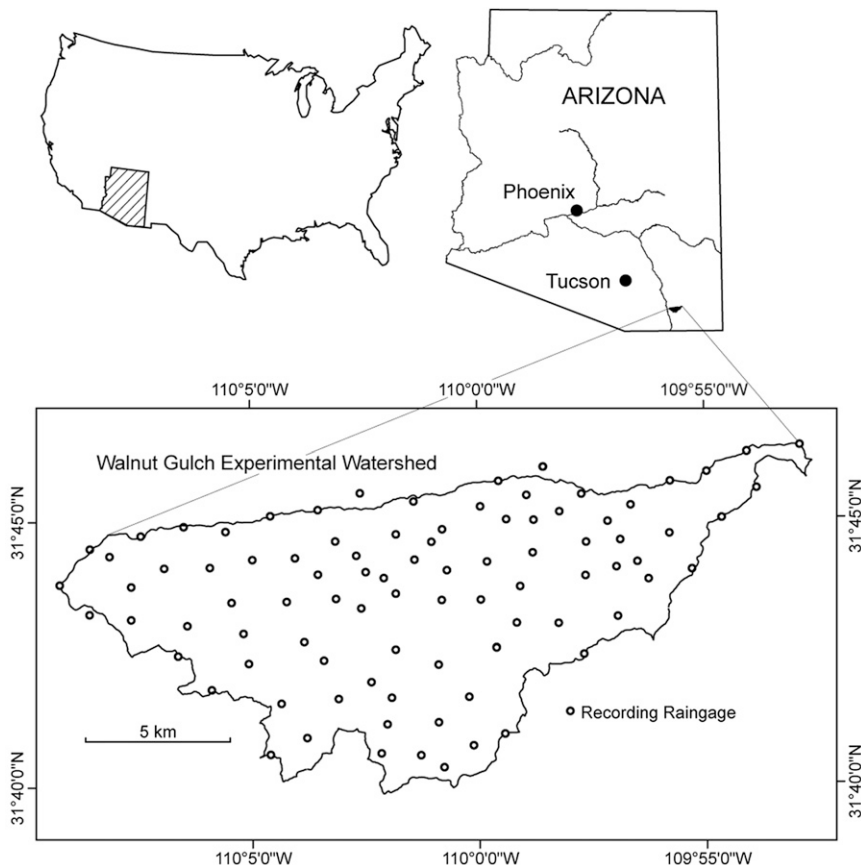
FIG. 1. The USDA-ARS Walnut Gulch Experimental Watershed (WGEW) location. The network consists of 88 weighing rain gauges within a 149 km^2 area.

United States. We compare instantaneous R fields from the TRMM precipitation radar (PR) (Iguchi et al. 2000) and interpolated gauge R fields. The comparisons are based on data from all TRMM overpasses in which the PR recorded rain within the boundaries of the WGEW. Special attention is given to the distance of the watershed from the TRMM subsatellite track. The closer the watershed is to the nadir line, the closer the PR observations are to the surface and thus are less affected by evaporation and wind displacement common in this environment.

2. The WGEW gauge network

The WGEW, operated by the U. S. Department of Agriculture, Agricultural Research Service (USDA-ARS), Southwest Watershed Research Center, encompasses 149 km^2 in southeastern Arizona, surrounds the historical western town of Tombstone, and drains to the outlet streamflow gauge at (31°43′N, 110°09′W). The WGEW is contained within the 7600-km^2 upper San Pedro River

basin. Elevation of the watershed ranges from 1250 to 1585 m MSL. The watershed receives approximately 350 mm of precipitation annually. Roughly 60% occurs during the summer monsoon as high-intensity air mass thunderstorms of limited spatial extent. Approximately 30% comes from less intense, spatially larger and more uniform winter frontal systems and approximately 5% from tropical depressions in the fall resulting in large-area, long-duration, heavy precipitation.

The network consists of 88 weighing rain gauges (Fig. 1) with 1-min reporting intervals during precipitation (Keefer et al. 2008). This constitutes one of the densest precipitation gauge networks in the world for an area greater than 10 km^2 (0.59 gauges km^{-2}, Garcia et al. 2008). By comparison, the area of the TRMM PR footprint [field of view (FOV)] is ~20 km^2 [the PR FOV diameter, or "3-dB beamwidth," at nadir is 4.3 km for preboost orbits (before 7 August 2001) and 5.0 km for postboost orbits (after 24 August 2001)]. Therefore, on average, approximately 10 gauges can be found in each PR FOV. Other existing gauge networks under the PR

coverage area do not reach such density. For example, a TRMM orbit over the NASA Kennedy Space Flight Center network in central Florida may include several PR FOVs, each with two to three gauges, and only one FOV, at a very unique PR footprint orientation, with four gauges (see Wang and Wolff 2010, Fig. 1). The other important and unique feature of the WGEW network is that all gauges are very well synchronized (datalogger clocks are reset to National Institute of Standards and Technology time every six months; average datalogger time drift between gauges is ± 4 s month^{-1} with a standard deviation less than 20 s month^{-1} and the maximum time difference between gauges is less than 30 s month^{-1}). This allows generating very high temporal-resolution R fields, and obtaining accurate estimates of the area-average R for the entire watershed and for a single TRMM PR FOV.

Very high temporal- (1 min) and spatial-resolution (100 m) rainfall rate maps were generated using the multiquadric–biharmonic (MQB) spatial interpolation scheme. Garcia et al. (2008) evaluated both the inverse-distance-weighted (IDW) and MQB schemes for the WGEW and found MQB superior. The high-resolution data allows for time/space shifting of the rain rate fields with respect to each other to account for the change in position of the hydrometers from which they were observed.

3. Results

a. Comparison of rain rates derived from satellite and gauges

The results presented in this paper are based on data from the TRMM 2A25 products, PR near-surface rainfall parameter (JAXA 2011; Iguchi et al. 2009). The products are based on the latest version of rain retrieval algorithms [version 7 (V7)], released in summer 2011. Comparisons with products based on the previous version, V6, are also presented, with the objective of evaluating whether V7 is better than V6. A description of the differences between V6 and V7 algorithms is provided in JAXA (2011). Major changes include a new correction formula of the nonuniform beam filling (NUBF) correction algorithm, which was disabled in V6; an improved attenuation correction algorithm based on a modified surface reference technique in which the total effect of the correction decreases; and a new drop size distribution (DSD) model for stratiform rainfall, which results in increase of the total stratiform rain. Initial comparisons indicate a decrease of the weak rain rates on a global scale and an increase of the convective intensities and of the total rainfall over land as we switch from V6 to V7.

The comparisons are based on data from all TRMM overpasses in which the PR recorded rain within the WGEW. Any overpass with at least one PR FOV with $R > 0$ centered within the watershed is defined as a "rainy" overpass. During 1999–2010, 25 rainy TRMM overpasses were found covering the watershed (two additional rainy overpasses were found during 1998, the first year of the TRMM mission, while the network consisted of analog gauges with mechanical clocks that did not have sufficient temporal synchronization and therefore are not used in this study). For four of the 25 overpasses analyzed in this study (three occurring in October and one in November) the gauge observations resulted from stratiform precipitation. The remainder occurred during the monsoon and resulted from convective precipitation.

Figure 2 provides an example of the rain rate fields for a rain event during 4 October 2001. The fields are for the PR V6 and V7 estimates and for the interpolated gauge rainfall rates (G) at 0, 5, and 10 min after the overpass time. The G field was derived every 1 min at 100-m resolution for a period of ± 30 min around the overpass time. The best agreement between the PR and the G fields is obtained several minutes after the overpass time when the most intense rain shifted west where the outlet of the watershed is located. Better agreement is obtained with V7. The peak intensity observed in V6 at the west edge has been reduced, and the weak intensities at the east and southeast of the watershed have been removed, resulting in a better match.

The 25 rainy TRMM overpasses include a total of 236 rainy PR FOVs covering the watershed: 108 centered within the watershed and 128 centered outside the watershed. The number of FOVs is slightly higher for V6. A different clutter rejection-filtering algorithm being used in V7 reduced the number of FOVs associated with weak rain intensities (as can be seen in Fig. 2). A FOV is considered to cover the watershed if it is the nearest FOV to at least one location inside the watershed. These 236 FOVs will be used to calculate the entire watershed area-average rainfall rate (section 3c). However, the results presented in this section and in section 3b are based on PR FOVs located almost entirely inside the watershed. Eighty-five out of the 108 rainy PR FOVs were found "entirely" within the watershed (80% of the FOV size was used as an area threshold to define a FOV that is entirely within the watershed). In Fig. 2, for example, four FOVs are found entirely within the watershed. They are located on the center row along the watershed. Each of them includes more rain gauges than any other FOV that is illustrated on this image, as can be seen by the number of red dots denoting the rain gauge locations.

Not all FOVs located entirely within the watershed were registering rain. The 25 TRMM overpasses include
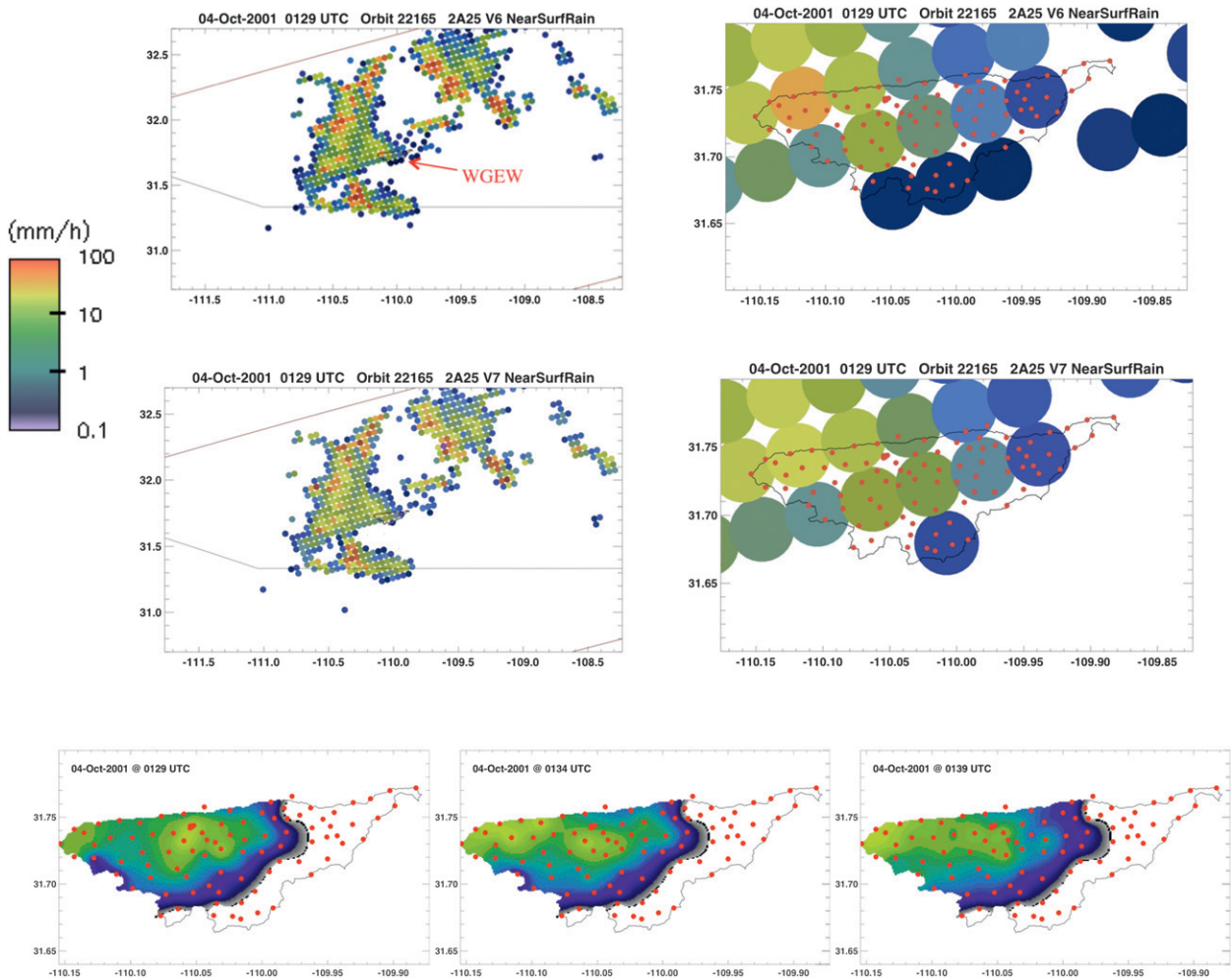
FIG. 2. The rain rate field as observed by the TRMM PR on 4 Oct 2001 at 0129 UTC (orbit 22 165) based on (top) version 6 (V6) and (middle) version 7 (V7) rain retrieval algorithms. The WGEW interpolated gauge rainfall rate fields (bottom) at 0, 5, and 10 min after the overpass. All fields have the same color scale. Each PR footprint (FOV) is illustrated schematically by a 5.0-km diameter circle. Each of the 88 gauges is marked by a red dot. Top-left and middle-left panels provide a wide field of view with the WGEW located at their center. The two red parallel diagonal lines mark the edge of the PR swath; the thin black line across the swath marks the U.S.–Mexico border.

136 PR FOVs located entirely inside the watershed; 88 of them with rain (61 with PR and G rain, 24 with PR rain only, and 3 with G rain only). These numbers are for V7 at 5 min after the overpass. The number of rainy pairs changes slightly for V6 (91). Figure 3 presents the correlation coefficients (CC) for the 88 PR/G FOV pairs (black curves), and the PR/G average rain rate ratio from all FOVs combined ($\Sigma R_{PR}/\Sigma R_G$) (gray curves) for every minute during an hour, centered at the overpass time. The number of pairs (88 for V7, 91 for V6) also changes slightly within the hour (88–96 for V7, 91–99 for V6) since the number of FOV with $G > 0$ changes. Each PR/G pair represents the PR FOV rain rate and G—the simulated PR FOV area-average rain rate using the high-resolution gauge field. The simulation is performed

by assigning each 100-m gauge pixel to its closest PR FOV, following simple averaging of all gauge pixels associated with the same FOV. In other words, for a given PR FOV all the gauge pixels within the watershed that are within a 5 km × 5 km square centered at the PR FOV are averaged. The maximum number of gauge pixels associated with a 5-km FOV is therefore $50 \times 50 = 2500$. As seen in Fig. 3, the correlation is high at overpass time, but the peak occurs several minutes after overpass time, which can be explained by the fact that it takes several minutes for the rain drops to reach the gauge from the time they are observed by the PR. During the time of maximum correlation the PR/G bias is about 1.1. At other times, its value is of less importance as it depends on the nature of the rainfall system.
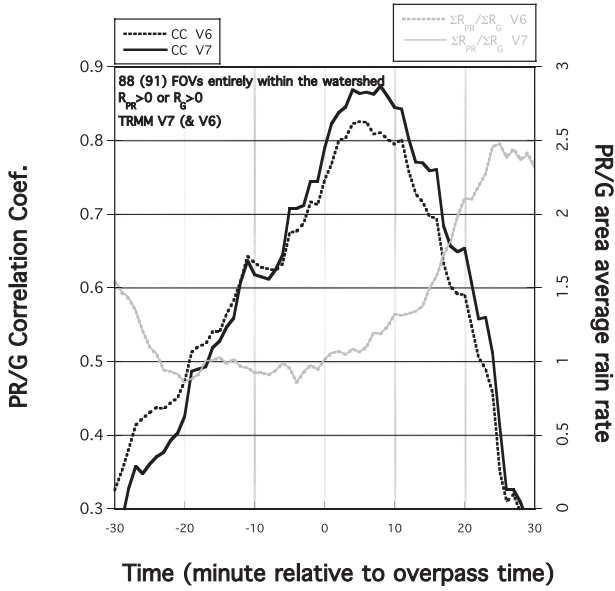
FIG. 3. The correlation coefficients (CCs) between the PR and *G* FOV rain rates (black curves), and the PR/*G* average rain rate ratio from all FOVs combined ($\Sigma R_{PR}/\Sigma R_G$) (gray curves), for every minute during an hour, centered at the overpass time. All FOVs located entirely inside the watershed that registered rain (PR or *G*) are analyzed. Each PR/*G* pair represents the PR FOV rain rate and *G* the corresponding area-average rain rate from all 100-m gauge pixels associate with the same FOV.
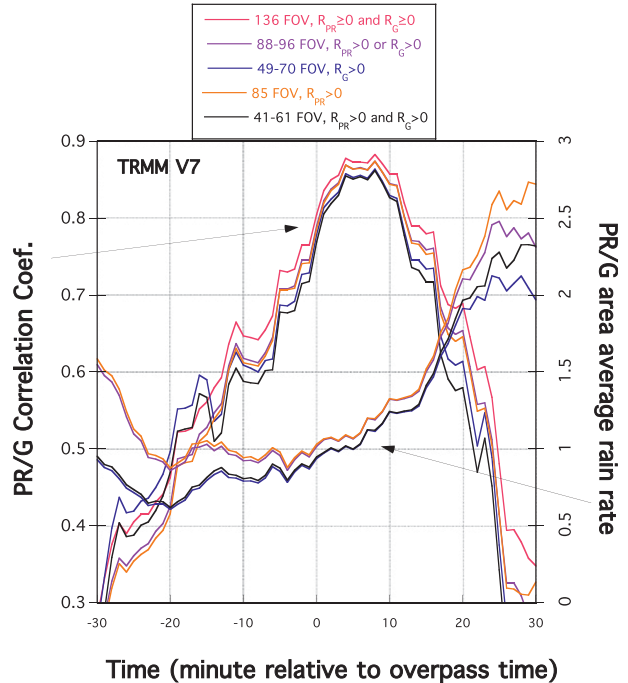

FIG. 4. The correlation coefficients between the PR/*G* FOV rain rates and the PR/*G* average rain rate ratio, as in Fig. 3, but for different conditional rain cases: PR V7 only.

Statistically, however, since we are selecting only rainy overpasses there is a higher probability that before/after the overpass it will be raining less than during the overpass time. Therefore, a PR/*G* curve that is based on a large number of overpasses is expected to have a minimum around the overpass time with a slope that is steeper as the average lifetime of the rain events is shorter. Such a curve is realized in Fig. 3 although the sample is small. Figure 3 suggests that higher CCs are obtained using V7 at least across the 30 min centered at the time of the CC maxima. The sum of the PR rain rates is, however, almost the same in V6 as with V7 ($\Sigma R_{PR\ V6} = \Sigma R_{PR\ V7}$). This is indicated in the figure by the fact that both gray curves overlay each other (i.e., since ΣR_{PR} is constant in time and *G* is independent of the PR version, for any given time *t* relative to the overpass time we will obtain $\Sigma R_{PR\ V6}/\Sigma R_{G,t} = \Sigma R_{PR\ V7}/\Sigma R_{G,t}$).

The analysis in this study is based solely on rainy overpasses; however, some FOVs within a rainy overpass may record no rain, and still will be used in the analysis. The 25 rainy overpasses include 136 TRMM PR FOVs (with $R \geq 0$), located entirely within the watershed. The CC analysis presented in Fig. 3 includes only FOVs that registered rain according to either PR or *G*. Figure 4, however, presents CC curves for different "conditional on rain" situations: 1) for no conditions

based on a rain threshold, 2) for FOVs that registered rain according to either PR or *G* (as in Fig. 3), 3) for rainy *G* FOVs, 4) for rainy PR FOVs, and 5) for FOVs that registered rain according to both the PR and the *G* fields. The CC might be misleadingly high if both instruments are measuring zero rain (rather common in such a semiarid environment). However, as seen in Fig. 4 the CC remains relatively high when no-rain FOVs are excluded. Similar results are obtained using V6, in which the peak CC values range from 0.82 to 0.83 for the different cases (not shown). In addition, Fig. 4 displays the $\Sigma R_{PR}/\Sigma R_G$ from all FOVs combined for the different conditional cases. At the time of the maxima CC, PR overestimates *G* by about 10%.

It is worth noting that the correlation coefficient statistic is usually subject to sampling uncertainties, especially when the sample size is small. The sampling distribution of the correlation coefficient is fairly well known when the underlying variables follow a normal distribution (Johnson et al. 1995). Much less is known about the sampling distribution in the case of skewed variables, such as the case with the PR and *G* rainfall estimates (Habib et al. 2001). However, given the relatively large values of CC reported in the current study, we do not expect the sampling effect on the estimation of CC to be large enough to change the conclusions about the strong association between the PR and *G* samples.
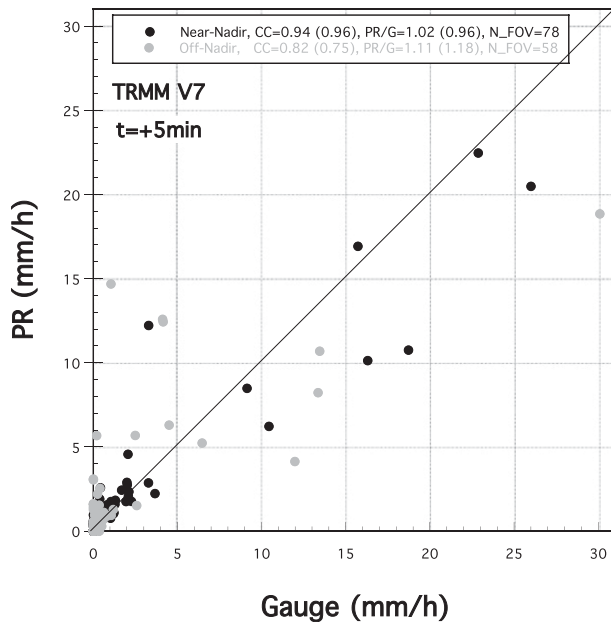
FIG. 5. The PR V7/G rain rate estimates at each PR FOV. All PR FOVs located entirely within the watershed (136) from all 25 rainy overpasses are included. The interpolated gauge rain rate field is based on measurements taken 5 min after the overpass time. The FOVs are classified into two groups according to their distance from the satellite nadir line. In addition to the correlation (CC), the legend displays the PR/G sum of rain rate ratio from all FOVs combined. Values in parentheses are for V6.

b. Classification by distance from TRMM nadir line

Special attention is given to the distance of each FOV from the TRMM subsatellite track. The closer the FOV is to the nadir line, the closer the PR observations are to the surface. The range resolution of the TRMM PR is 250 m, which is equal to the vertical resolution at nadir. However, as the scanning cross-track angle increases toward the swath edge (18°) the effective vertical range of the (5 km × 0.25 km) tilted disk spans 1.8 km vertically (for an illustrative figure see Bolen and Chandrasekar 2003). Figure 5 consists of a scatterplot of the PR V7/G rain rate estimates at each PR FOV. All 136 PR FOVs located entirely within the watershed are included. The interpolated gauge rain rate field is based on measurements taken 5 min after the overpass time, which is about the time when the highest correlation was obtained based on all FOVs (when taking into account results from both V6 and V7). The FOVs are classified into two groups according to their distance from the satellite nadir line. Across the PR swath 49 FOVs exist. For this analysis, the inner 25 FOVs (associated with scanning cross-track angles range from 0° to 9°) have been defined as "near nadir" while the others are denoted as "off nadir." The near-nadir group includes 78 FOVs based on 15 overpasses,

TABLE 1. Contingency table for TRMM PR 2A25 (V7) surface rain rate FOVs (R_{PR}) and the simulated PR FOVs using the high-resolution gauge-based rain rate fields (R_G) at 5 min postoverpass. The table is based on the 136 FOVs presented in Fig. 5. The first number is for near nadir; the number in parentheses is for all FOVs (near nadir + off nadir). FOVs with $R_G < 0.05$ mm h^{-1} have been defined for this study as $R_G = 0$ mm h^{-1}.

	$R_G = 0$	$R_G > 0$	Total
$R_{PR} = 0$	32 (48)	0 (3)	32 (51)
$R_{PR} > 0$	13 (24)	33 (61)	46 (85)
Total	45 (72)	33 (64)	78 (136)

and the off-nadir 58 FOVs based on 13 overpasses. Three overpasses had both near- and off-nadir FOVs. The correlation between PR and G is noticeably higher for FOVs that are closest to the TRMM nadir line (black dots) than those farther from the nadir line (gray dots). The figure presents several wet-PR/dry-G FOVs (i.e., $R_{PR} > 0$ and $R_G = 0$). Most of these are off-nadir FOVs with weak PR rain rates, which probably are affected by evaporation. The off-nadir FOVs might also be subject to larger space/time displacement than the near-nadir FOVs. Hardly any dry-PR/wet-G FOVs exist. The legend in Fig. 5 displays the PR/G correlation coefficient and average rain rate ratio ($\Sigma R_{PR}/\Sigma R_G$). Values in parentheses are for V6. All values are for 5-min postoverpass. In V7 (versus V6) the CC is higher for the off-nadir FOVs, and a bit lower for the near-nadir FOVs. For all FOVs combined the peak CC value is higher in V7 (Fig. 3). The bias is reduced in V7. Although the overall PR/G bias remains almost the same (Fig. 3), the PR near-nadir underestimation and off-nadir overestimation are reduced (from 0.96 to 1.02 and from 1.18 to 1.11 for the near-nadir and off-nadir FOVs, respectively).

Table 1 summarizes the contingency table for the FOVs presented in Fig. 5. The number of wet-PR/wet-G FOVs is much higher than the number of wet-PR/dry-G FOVs or the number of dry-PR/wet-G FOVs. For example, excluding cases of dry-PR/dry-G FOVs, 72% of the near-nadir FOVs correspond to instances when rainfall was detected by both PR and G, 28% by PR only, and 0% by G only. Prat and Barros (2010) is the only other study, we are aware of, that compares snapshots of TRMM PR and gauge rain rate measurements. Their study is based on a large number of TRMM overpasses over a much less dense network in the southern Appalachian Mountains. The gauge rain rates were averaged over several time periods, but no spatial interpolation was performed. Their comparison with 10-min point rain gauge rain rates centered over the time the satellite overpasses results with a very low correlation of $r^2 = 0.03$ ($r^2 = 0.14$ for nonnull records)—see Fig. 4 in their manuscript. They also present a contingency table. Excluding cases in
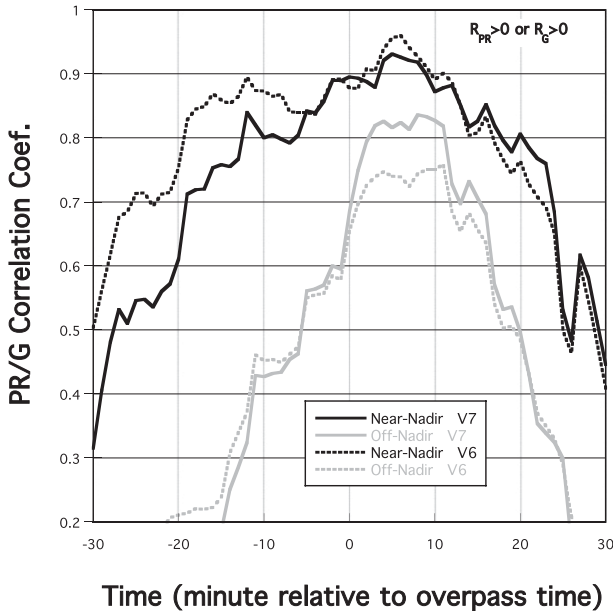
FIG. 6. The correlation coefficients between the PR/G FOV rain rates, as in Fig. 3, but upon classification by the distance of each FOV from the satellite nadir line.
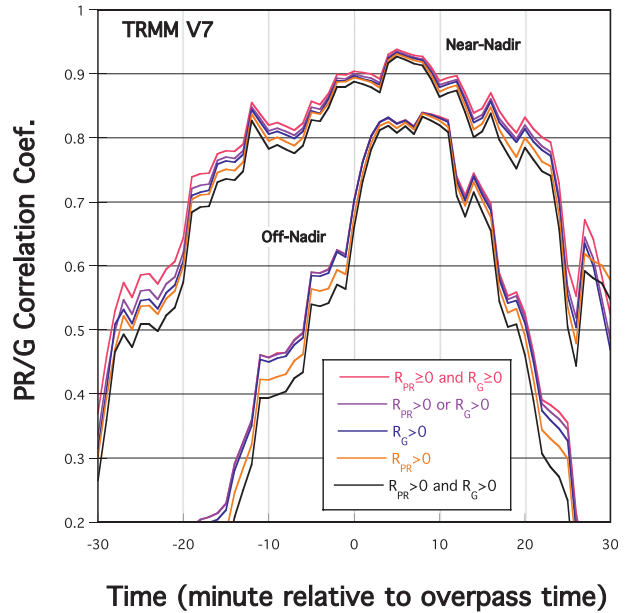

FIG. 7. The correlation coefficients between the PR/G FOV rain rates for different conditional rain cases, as in Fig. 4, but upon classification by the distance of each FOV from the satellite nadir line.

which both PR and gauge observed no rain, only 30% of all PR/G pairs corresponded to instances when rainfall was detected by both PR and G, 20% by PR only, and 50% by G only. This large mismatch, they suggest, might be due to limited performance of the gauge network or to PR sensitivity.

In Fig. 5 the simulated PR FOVs are based on measurements taken 5 min after the overpass time. Figure 6 presents the CCs between the PR/G FOV rain rates for every minute during an hour, centered at the overpass time, as in Fig. 3, but upon classification of the FOVs by their distance from the satellite nadir line. A clear separation between the two classes exists. The double peak observed in the correlation curve for all the FOVs combined at $t = 4$ min and $t = 8$ min of CC = 0.88 (Fig. 3) can be viewed as a convolution of a single peak of CC = 0.93 at $t = 4$–5 min for the near-nadir FOVs and a wide spread maxima at 3-min $< t <$ 11 min of about CC = 0.83 for the off-nadir FOVs. In other words, as we move off nadir the correlation decreases and the peak becomes broader. This is perhaps expected since the farther the PR FOV is from the nadir line, the volume it samples has a larger vertical range and, therefore, precipitation from that volume will reach the surface over a longer time period. Near the nadir line the height of the FOV being converted from reflectivity to rain rate varies according to the topography, and is found on average to be 3–4 gates or 750–1250 m above ground level. A 4–5-min fall time from such heights corresponds to drop velocities of 3–5 m s^{-1}, which are

typical terminal velocities for small raindrops in convective rainfall or medium raindrops in stratiform rainfall (e.g., Niu et al. 2010, and references within).

Figure 7 presents the CCs between the PR/G FOV rain rates for different conditional rain cases, as in Fig. 4, but upon classification by the distance of each FOV from the satellite nadir line. As in the previous figure, a clear separation between the near-nadir and the off-nadir correlation curves exists. As in Fig. 4, the CCs are insensitive to the conditional on rain case.

c. Watershed area-average rainfall rate

Previous sections presented FOV-by-FOV correlations and integrated rainfall rate ratios ($\Sigma R_{PR}/\Sigma R_G$) for several overpasses, which were combined, based on FOVs located entirely within the watershed. This section presents results from calculating the entire watershed area-average rainfall rate for each overpass separately. The area-average rain rate is calculated by relating each 100-m pixel that is located within the watershed to its nearest PR FOV, regardless whether the FOV center is inside or outside the watershed. As mentioned in section 3a, this comprises 236 rainy PR FOVs, as opposed to only 85 located entirely within the watershed. Figure 8 presents the PR/G area-average rainfall rate for each of the 25 overpasses during the overpass time and for each minute during the 15 min following each overpass. Therefore, a given overpass is associated with points having the
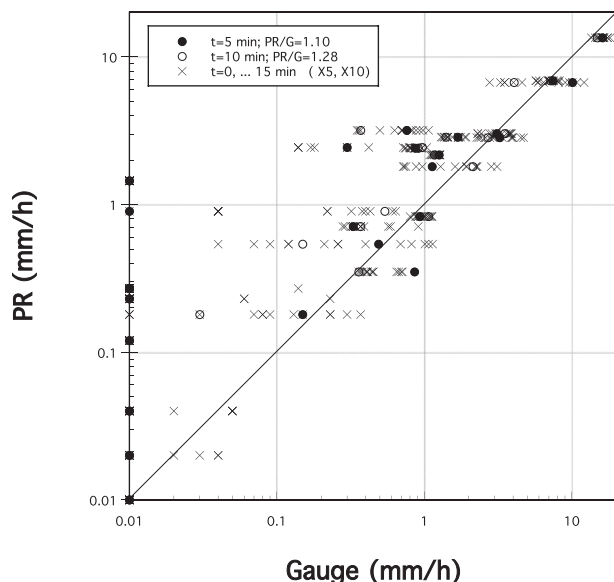
FIG. 8. The PR/G area-average rain rate for the entire watershed for each overpass. The gauge area-average rain rate is calculated for the overpass time and for each minute during the 15 min following the overpass. The values at 5 and 10 min after the overpass time are marked separately. Zero rain rate values were defined as 0.01 mm h^{-1} to allow presentation of data on a logarithmic scale.

same PR R value, and therefore appears in Fig. 8 as horizontal series of ×s and dots ("horizontal line"). Zero rain rate values were defined as 0.01 mm h^{-1} to allow presentation of data on a logarithmic scale. In 15 out of the 25 overpasses the area-average rain rate of PR and G matches during some moment within the 15-min window. This can be seen in the figure by the number of horizontal lines crossing the 1:1 line. The watershed is positioned in both near-nadir and off-nadir regions in these 15 overpasses (these include 6 out of the 12 overpasses in which the watershed is positioned in the near-nadir region, 6 out of the 10 overpasses in which the watershed is positioned in the off-nadir region, and 3 out of the 3 overpasses in which the watershed contains FOVs in both near- and off-nadir regions). We should not expect the area-average rain rate of PR and G to match in each overpass for several reasons. First, in this semiarid environment raindrops are subject to evaporation. This is supported by the relative high numbers of cases of wet PR/dry G and by the overestimation of the PR relative to G for the off-nadir FOVs (Fig. 5) and for the entire watershed (Fig. 8). Second, wind induced undercatch of rainfall by the gauge (e.g., Nespor and Sevruk 1999; Chvíla et al. 2005). Third, this is a small watershed in terms of number of FOVs entirely within the watershed relative to the number of FOVs that partially cover the watershed. In calculating the entire watershed

area-average rainfall rate many pixels are assigned the PR rain rate value of FOVs centered outside the watershed. Finally, wind displacement of the raindrops affects the area-average rainfall rate of small watersheds. Preliminary analysis indicates that shifting the PR/G fields with respect to each other not only in time, as presented here, but also in space will result in improved FOV-by-FOV correlation and improved area-average rain rate agreement (not shown). While the aforementioned factors are suggested as primary reasons for expecting some bias between PR and G, many other factors may have contribute to the bias ratio. Among these are gauge *settings* and their spatial distribution, spatial and temporal variability of the rainfall, uncertainties of PR rain rate estimates related to DSD, attenuation correction errors, NUBF effects fillings, topography, and other factors (Iguchi et al. 2009).

d. Assessment of the accuracy of the reference products

In this study, the PR estimates are evaluated using reference ground observations from rain gauges. There are on average about 10 rain gauges within a single PR FOV, and it is thus assumed that the average of observations from the multiple gauges located within each FOV provides a reliable approximation of the unknown true surface rainfall. The accuracy of such approximations will depend on the number and configuration of gauges within the FOV and on the degree of subpixel rainfall natural spatial variability. The adequacy of the number of gauges within the FOVs is examined by calculating the error variances of the FOV gauge-average approximations using a well-established statistical measure: the variance reduction factor (VRF) (Bras and Rodriguez-Iturbe 1993). The VRF provides a relative measure of the variance of the error associated with approximating the unknown true area-average rainfall over the scale of the PR FOV when using a certain number and configuration of gauges within the area of interest. Calculations of the VRF require specification of the rainfall spatial correlation function over the study area. We used results from the correlation analysis of Morin et al. (2003), which were done for the same watershed to estimate the spatial correlation function of 1-min rainfall rates. The VRF is computed for a representative FOV within which 10 gauges are uniformly distributed. For comparison, the VRF is also computed for hypothetical cases of other gauge densities that range from a single gauge located in the center of the FOV to 15 gauges with a fairly uniform distribution within the FOV. The results are plotted in Fig. 9 and indicate a significant drop (i.e., improvement) in the VRF as the number of gauges is increased up to five gauges but levels off
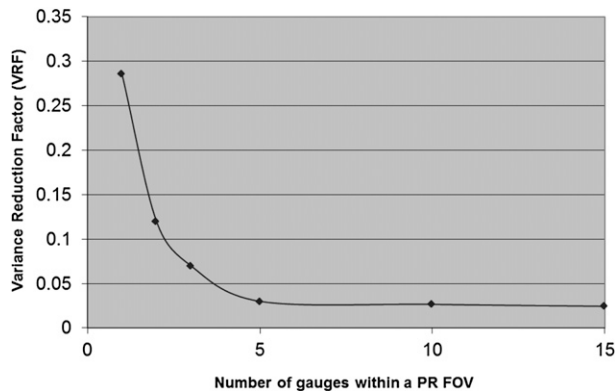
FIG. 9. The variance reduction factor (VRF) for different gauge densities with a fairly uniform distribution. The VRF is calculated using the spatial correlation function of 1-min rainfall rates, which was estimated from the results of Morin et al. (2003) for the same watershed.

rapidly beyond five gauges for which little or no improvement is observed. The VRF under the gauge density used in the current study (about 10 gauges per FOV) has a value of 0.0286, which is about 10 times less (i.e., more accurate) than the VRF under a single-gauge situation (VRF = 0.27). Overall, these results indicate that, when 10 gauges are available in the FOV, the gauge-representativeness errors are significantly reduced compared to typical cases when only a lower number of gauges is available. Thus it is reasonable to conclude that the uncertainties caused by using the current number of gauges in each FOV do not contribute in any tangible way to the observed differences between the PR estimates and the gauge-based fields.

Another possible source of gauge-induced uncertainties may arise from the method used to interpolate point observations into area-average estimates. However, such uncertainties are expected to be of less importance especially with the availability of several gauges within the FOV and the relatively small size of the FOV area itself.

These results have important implications for the current and future studies that deal with assessment of satellite rainfall estimates using limited number of gauges. In the current study, the number of gauges available per FOV falls beyond the part of the VRF curve where the gauge representativeness errors are still large. However, in other cases where a smaller number of gauges are used (i.e., less than five gauges per FOV), as is typically encountered in most satellite–gauge comparisons, the gauge uncertainties can significantly contribute to the gauge−satellite differences. This, in turn, can adversely affect any conclusions about the quantification and statistical characterization of satellite estimation errors. While the behavior of the VRF function plotted in Fig. 9 is

probably specific to the current study site, similar behavior is expected in other regions with pronounced levels of rainfall small-scale natural variability. As such, it is critical that any future satellite–gauge comparisons are preceded by some level of analysis to quantify the expected effect and contribution of gauge-induced uncertainties.

4. Closing remarks

The dense gauge network of the USDA-ARS Walnut Gulch Experimental Watershed in southeastern Arizona provides a unique opportunity for assessing rain rate retrievals from remote sensing observations. Instantaneous rain rate fields (snapshots) from TRMM PR and spatially interpolated gauge measurements (on a 100 m × 100 m grid, updated every 1 min) were compared for 25 rainy overpasses, which occurred during 1999–2010.

Results indicate a very good agreement between the fields with high correlation and low bias values, especially for the near-nadir cases (CC > 0.9); values this high are typically not observed when comparing remote sensing observations (i.e., satellite versus ground radar rainfall rate fields). The correlation is high at overpass time, but the peak occurs several minutes after the overpass, which can be explained by the fact that it takes several minutes for the raindrops to reach the gauge from the time they are observed by the TRMM PR.

Results suggest that the WGEW network provides a good platform to evaluate different TRMM PR rain retrieval algorithms. Results indicate improvement using V7. In V7 (versus V6) the CCs are higher overall and for off-nadir cases. However, for the near-nadir cases the peak CCs values are a bit lower for V7. In V7 the bias is also reduced. Although the overall PR/G bias remains almost the same, the PR near-nadir underestimation and off-nadir overestimation are reduced.

Spatial correlation analysis indicates uncertainties caused by using 10-gauge averages apparently do not contribute in any tangible way to the observed differences between PR and the gauge-based G fields used in this analysis.

In this example, the fields were shifted in time only. Future work will test shifting in space and in time to account for the displacement. Preliminary results suggest that shifting in time and space is required to obtain the highest correlations. Spatial shifting depends on the wind speed/direction and, therefore, might be different from overpass to overpass. Future work will also attempt to further understand the discrepancies between satellite and in situ observations. Utilizing the PR high-resolution vertical reflectivity structure and the NEXRAD observations over the watershed (the latter unfortunately suffer from some mountain blockage at low scan angles) should be considered.

REFERENCES

Bolen, S. M., and V. Chandrasekar, 2003: Methodology for aligning and comparing spaceborne radar and ground-based radar observations. *J. Atmos. Oceanic Technol.,* **20,** 647–659.

Bras, R. L., and I. Rodriguez-Iturbe, 1993: *Random Functions and Hydrology.* Dover, 559 pp.

Chvíla, B. B. S., B. Sevruk, and M. Ondrás, 2005: The wind-induced loss of thunderstorm precipitation measurements. *Atmos. Res.,* **77** (1–4), 29–38, doi:10.1016/j.atmosres.2004.11.032.

Garcia, M., C. D. Peters-Lidard, and D. C. Goodrich, 2008: Spatial interpolation of precipitation in a dense gauge network for monsoon storm events in the southwestern United States. *Water Resour. Res.,* **44,** W05S13, doi:10.1029/2006WR005788.

Goodrich, D. C., T. O. Keefer, C. L. Unkrich, M. H. Nichols, H. B. Osborn, J. J. Stone, and J. R. Smith, 2008: Long-term precipitation database, Walnut Gulch Experimental Watershed, Arizona, United States. *Water Resour. Res.,* **44,** W05S04, doi:10.1029/2006WR005782.

Habib, E., W. F. Krajewski, and G. J. Ciach, 2001: Estimation of inter-station correlation coefficient in rainfall data. *J. Hydrometeor.,* **2,** 621–629.

Iguchi, T., T. Kozu, R. Meneghini, J. Awaka, and K. Okamoto, 2000: Rain-profiling algorithm for the TRMM precipitation radar. *J. Appl. Meteor.,* **39,** 2038–2052.

——, ——, J. Kwiatkowski, R. Meneghini, J. Awaka, and K. Okamoto, 2009: Uncertainties in the rain-profiling algorithm for the TRMM precipitation radar. *J. Meteor. Soc. Japan,* **87A,** 1–30.

JAXA, cited 2011: PR algorithm and product information. [Available online at http://www.eorc.jaxa.jp/TRMM/documents/PR_algorithm_product_information/top_e.html.]

Johnson, N. L., S. Kotz, and N. Blakrishnan, 1995: *Continuous Univariate Distributions.* 2nd ed. Wiley Series in Probability and Mathematical Statistics, Vol. 2, John Wiley and Sons, 752 pp.

Keefer, T. O., C. L. Unkrich, J. R. Smith, D. C. Goodrich, M. S. Moran, and J. R. Simanton, 2008: An event-based comparison of two types of automated-recording, weighing bucket rain gauges. *Water Resour. Res.,* **44,** W05S12, doi:10.1029/2006WR005841.

Kummerow, C., W. Barnes, T. Kozu, J. Shiue, and J. Simpson, 1998: The Tropical Rainfall Measuring Mission (TRMM) sensor package. *J. Atmos. Oceanic Technol.,* **15,** 809–817.

Morin, E., W. F. Krajewski, D. C. Goodrich, X. Gao, and S. Sorooshian, 2003: Estimating rainfall intensities from weather radar data: The scale-dependency problem. *J. Hydrometeor.,* **4,** 782–797.

Nespor, V., and B. Sevruk, 1999: Estimation of wind-induced error of rainfall gauge measurements using a numerical simulation. *J. Atmos. Oceanic Technol.,* **16,** 450–464.

Niu, S., X. Jia, J. Sang, X. Liu, C. Lu, and Y. Liu, 2010: Distributions of raindrop sizes and fall velocities in a semiarid plateau climate: Convective versus stratiform rains. *J. Appl. Meteor. Climatol.,* **49,** 632–645.

Prat, P. O., and A. P. Barros, 2010: Assessing satellite-based precipitation estimates in the Southern Appalachian mountains using rain gauges and TRMM PR. *Adv. Geosci.,* **25,** 143–153, doi:10.5194/adgeo-25-143-2010.

Wang, J., and D. B. Wolff, 2010: Evaluation of TRMM ground-validation radar-rain errors using rain gauge measurements. *J. Appl. Meteor. Climatol.,* **49,** 310–324.